

Where is the fuzz? Undetected Lyman α nebulae around QSOs at $z \sim 2.3^*$

Edmund Christian Herenz¹, Lutz Wisotzki¹, Martin Roth¹, and Friedrich Anders¹

Leibniz-Institut für Astrophysik Potsdam (AIP)
An der Sternware 16, 14482 Potsdam e-mail: cherenz@aip.de

Received ...; accepted: 17 February 2014

ABSTRACT

We observed a small sample of 5 radio-quiet QSOs with integral field spectroscopy to search for possible extended emission in the Ly α line. We subtracted the QSO point sources using a simple PSF self-calibration technique that takes advantage of the simultaneous availability of spatial and spectral information. In 4 of the 5 objects we find no significant traces of extended Ly α emission beyond the contribution of the QSO nuclei itself, while in UM 247 there is evidence for a weak and spatially quite compact excess in the Ly α line at several kpc outside the nucleus. For all objects in our sample we estimated detection limits for extended, smoothly distributed Ly α emission by adding fake nebulosities into the datacubes and trying to recover them after PSF subtraction. Our observations are consistent with other studies showing that giant Ly α nebulae such as those found recently around some quasars are very rare. Ly α fuzz around typical radio-quiet QSOs is fainter, less extended and is therefore much harder to detect. The faintness of these structures is consistent with the idea that radio-quiet QSOs typically reside in dark matter haloes of modest masses.

Key words. galaxies: quasars: emission lines – galaxies: high-redshift
galaxies: quasars: individual: UM 247, Q 0027+0103, Q 0256-0003, Q 0308+0129, Q 2243+0141,

1. Introduction

The circum-galactic medium (CGM), defined as gas outside of the main stellar body of galaxies but still within the virial radii of their dark-matter haloes, is of crucial importance in galaxy evolution. It may act as a reservoir for fuelling star formation in the galaxy, and it is also subject to feedback processes that expell material from the galaxy. If violent enough, this feedback may in turn heat up the CGM and thus prevent it from contributing further to the formation of stars. Observing the CGM at high redshifts will hence provide relevant insights about galaxy formation.

One observational approach to study the ‘cold’ gas phase of the CGM ($T \lesssim 10^4$ K) at high redshift uses absorption signatures against background sources. This has provided important statistical constraints on several properties of the CGM (e.g. Adelberger et al. 2005; Hennawi et al. 2006; Steidel et al. 2010). However, the spatial distribution of the CGM in individual galaxy cannot be captured with this method.

An alternative approach is to map the CGM in the Lyman α emission line. Several mechanisms have been identified that should lead to Ly α emission from the CGM: Cooling of infalling gravitationally heated gas (e.g., Haiman et al. 2000), cooling following superwind-driven shocks (e.g., Taniguchi & Shioya 2000) and – possibly most important for our investigation – Ly α fluorescence induced by exposure to UV radiation. While the metagalactic UV background alone is predicted to produce only a very faint glow that is probably out of reach for the current generation of optical instruments (e.g., Kollmeier et al. 2010), Ly α

fluorescence caused by the much stronger UV radiation from a QSO should boost the emission into the detectable regime (Rees 1988; Haiman & Rees 2001; Kollmeier et al. 2010). Searching for Ly α signatures of the CGM around luminous QSOs is the topic of the present study.

Haiman & Rees (2001) estimated that a $z \sim 3$ QSO harbouring a $5 \times 10^{11} M_{\odot}$ halo should be surrounded by Ly α fuzz extending radially outwards to $2''$ – $3''$, at a surface brightness of $\sim 5 \times 10^{-17} \text{ erg s}^{-1} \text{ cm}^{-2} \text{ arcsec}^{-2}$. At least in this model, Ly α fuzz is predicted as a generic property of high- z QSOs, where the surface brightness of this fuzz depends only on the mass of the halo. More recent theoretical work suggests, however, that a substantial fraction of gas is accreted within filamentary cold streams (Dekel et al. 2009; Faucher-Giguère & Kereš 2011; Rosdahl & Blaizot 2012, and references therein). If these streams are optically thick to ionizing radiation, they will develop a highly ionized skin in the presence of a quasar. This skin then acts like a mirror converting up to two thirds of the incident ionizing radiation into Ly α photons. In this scenario the expected surface brightness then depends on the ionizing photon flux produced by the quasar and the projected spatial configuration of the streams (Kollmeier et al. 2010; Hennawi & Prochaska 2013).

Revealing extended Ly α structures around QSOs requires a proper subtraction of the PSF-broadened nuclear component, which will outshine – even under good seeing conditions – the expected CGM signal close to the QSO. Observationally, this makes the detection of circum-QSO Ly α fuzz much harder than searching for Ly α ‘blobs’, now routinely found in large-area narrow-band surveys (Steidel et al. 2000; Matsuda et al. 2004; Saito et al. 2006; Ouchi et al. 2009; Matsuda et al. 2011; Erb et al. 2011; Prescott et al. 2012, 2013). Many of these ‘blobs’ have no obvious central source of ionizing photons (e.g., Nils-

* Based on observations collected at the Centro Astronómico Hispano Alemán (CAHA) at Calar Alto, operated jointly by the Max-Planck Institut für Astronomie and the Instituto de Astrofísica de Andalucía (CSIC)

son et al. 2006), which might make them physically distinct from circum-QSO Ly α fuzz. On the other hand, some Ly α blobs may also be powered by AGN that are highly obscured along the line of sight (e.g. Basu-Zych & Scharf 2004; Geach et al. 2007; Hayes et al. 2011; Martin et al. 2014b); such blobs would be physically linked to the fuzz we want to observe (see also Baek & Ferrara 2013).

As of yet, sizeable samples of extended Ly α emission around QSOs exist only for radio-loud objects (Heckman et al. 1991a,b), for which such emission seems to be a generic property at $z \sim 2-3$, with detections reported up to $z \sim 6$ (Roche et al. 2014). However, it appears likely that a large fraction of extended Ly α emission around radio loud quasars is driven by interaction with the radio jets. Evidence for this stems from an observed spatial correlation between radio and Ly α morphology (e.g., Heckman et al. 1991b; Humphrey et al. 2007) and a frequent occurrence of similar morphologies in extended C IV and He II emission (Humphrey et al. 2006; Sánchez & Humphrey 2009).

In order to search for the CGM in QSOs unaffected by radio jets, one obviously has to resort to radio-quiet objects. For this class, however, mostly single object discoveries have been published so far (Bergeron et al. 1999; Bunker et al. 2003; Weidinger et al. 2004, 2005; Francis & McDonnell 2006; Willott et al. 2011; Goto et al. 2012; Rauch et al. 2013; Cantalupo et al. 2014; Martin et al. 2014a), and only one single-object study reported a non-detection at a faint surface-brightness detection limit (Francis & Bland-Hawthorn 2004). Very few programmes aimed at observing (however small) samples (Christensen et al. 2006; Courbin et al. 2008; North et al. 2012), and these reported high detection frequencies of circum-QSO Ly α -fuzz: Christensen et al. (2006) found Ly α fuzz around 4 of 6 radio-quiet QSOs, while North et al. (2012), by extending the sample of Courbin et al. (2008), found Ly α fuzz around 4 of 6 targets. So the literature suggests that Ly α fuzz is indeed a rather generic feature and not a peculiarity around high-redshift radio-quiet QSOs, even if the number of systematically observed QSOs appears still too low for certainty.

A major increase in sample size was recently achieved due to the work of Hennawi & Prochaska (2013). In a long-slit campaign on 8m-class telescopes they observed 29 close quasar-quasar pair sightlines, where Lyman-limit absorption in the background quasar spectrum indicated the presence of optically thick hydrogen clouds in the CGM of the foreground $z \sim 2$ radio-quiet quasars. The a priori known presence of such gas clouds implies that the sample would be positively biased for detecting ‘mirrored’ Ly α fuzz converted from the quasars ionizing photons (see above). They find a single quasar surrounded by a large scale nebula and 10 objects surrounded by small scale Ly α fuzz. Surprisingly, none of their spectra showed Ly α fuzz with the properties expected for optically thick ‘Ly α mirrors’.

For a survey on circum-QSO Ly α fuzz, integral-field spectroscopy is an optimal observational method since it has continuous spatial and spectral coverage. This technique allows for an optimal subtraction of the PSF-broadened nuclear emission. Moreover, since spatial and spectral information are obtained simultaneously in case of a detection, more inferences on the physical state of the CGM gas can be made. Given the previous success of a Calar-Alto 3.5m PMAS IFU campaign where 4 extended Ly α nebulae were detected around 6 radio-quiet QSOs (Christensen et al. 2006) (hereafter CJW06), we initiated a new targeted PMAS IFU campaign to extend this sample.

The outline of this paper is as follows: In Sect. 2 we describe our PMAS observations and how we reduced the raw data. In Sect. 3 we explain how we remove the QSO emission from the

datacubes to unveil possible extended Ly α nebulae. We detail how we estimate surface brightness upper limits in Sect. 3.3 and present the results of those calculations. We summarise our conclusions in Sect. 4.

Conversions of observed to physical quantities always assume standard Λ CDM cosmology with $\Omega_{\Lambda} = 0.7$, $\Omega_M = 0.3$ and $H_0 = 70 \text{ km s}^{-1} \text{ Mpc}^{-1}$.

2. Observations & Data Reduction

2.1. Sample selection & observations

Our sample was selected to be at redshifts around $z \sim 2.3$ so that, in the case of a successful detection of extended Ly α fuzz, spectroscopic follow-up observations of rest-frame optical emission lines would be possible. Starting from the Véron-Cetty & Véron (2010) catalog with this constraint, we browsed through all bright ($m_V > 19$ as in Véron-Cetty & Véron (2010)) radio-quiet QSOs at approximately the above redshift. In the end we were able to observe 5 of these targets with the Potsdam Multi-Aperture Spectrophotometer (PMAS; Roth et al. 2005) at Calar Alto Observatory during 3 consecutive cloudless dark- to grey-time nights in October 2011. Table 1 lists the redshifts and the SDSS u and g band magnitudes of our observed QSOs.

We used PMAS in its 16×16 lens array (LArr) configuration, giving an $8'' \times 8''$ field of view (FoV), (i.e. at $0.5'' \times 0.5''$ spatial sampling). Motivated by the increased sensitivity and larger spectral coverage of the upgraded PMAS detector (Roth et al. 2010), we mounted the V1200 grating to obtain the highest possible spectral resolution within the targeted wavelength range. The CCD was read out unbinned in dispersion direction. Exposure times, seeing, airmasses and observing conditions of our observations are listed in Table 1. To ensure the best possible spectral tracing and wavelength calibration we flanked each on-target exposure by continuum and HgNe lamp exposures. At the beginning and end of each night we observed an Oke (1990) spectrophotometric standard star (BD+24d4655 and G191B2B, respectively). We obtained skyflats during twilight and several bias frames during the night in idle time (e.g. while performing acquisitions).

2.2. Data reduction with p3d

To reduce the observations we employed the p3d-pipeline¹ (Sandin et al. 2010, 2012). We briefly outline in this section how we applied the different tasks of the pipeline to our data.

For every observing night a masterbias was created with the routine `p3d_cmbias`. The `p3d_ldmask` task then produced dispersion solutions for every arc-lamp frame, fitting 5th order polynomials for the mapping from pixel- to wavelength space; measured residuals for all arc lines were $\leq 10^{-1} \text{ px}$. To determine spectrum traces and cross-dispersion profiles we applied the `p3d_ctrace` method to every continuum lamp frame. We created wavelength calibrated flatfields using `p3d_cflatf`. The `p3d_cobjex` task then performed extraction, flat-fielding, and subsequent wavelength calibration of every target and standard star exposure. As detailed by Sandin et al. (2010), the best signal-to-noise for PMAS LArr spectra is achieved by using the modified optimal extraction (MOX) algorithm (Horne 1986). Due to the large separation of LArr fiber traces on the CCD, cross-talk correction between fibers is not needed. Sandin et al. (2012) advises correcting for small spectra trace shifts between

¹ <http://p3d.sourceforge.org>

Table 1. Observed radio-quiet QSOs: Properties, exposure Times & observing conditions.

| QSO | z_{VC} | z_{SDSS} | u_{SDSS} | g_{SDSS} | t_{exp} [s] | Seeing ["] | Airmass | Conditions |
|------------|----------|------------|------------|------------|---------------|------------|---------|---------------------|
| Q0027+0103 | 2.310 | 2.313 | 19.27 | 18.50 | 7×1800s | 0.9-1.3 | 1.2-1.6 | photometric / grey |
| Q0308+0129 | 2.335 | – | 19.21 | 18.45 | 7×1800 | 1.0-1.4 | 1.2-1.5 | mainly clear / dark |
| Q0256–0003 | 2.381 | 2.385 | 20.13 | 19.41 | 8×1800+1×900 | 0.9-1.1 | 1.3-1.6 | photometric / dark |
| Q2243+0141 | 2.314 | – | 18.48 | 17.98 | 8×1800 | 0.9-1.2 | 1.3-1.5 | photometric / grey |
| UM 247 | 2.333 | 2.333 | 18.85 | 18.10 | 5×1800s | 0.9-1.1 | 1.2-1.4 | photometric / dark |

Notes. Redshifts from Véron-Cetty & Véron (2010) (z_{VC}); and Pâris et al. (2012) (z_{SDSS}). Photometry from Ahn et al. (2012).

continuum-lamp and on-target exposures for achieving highest fidelity with MOX extraction, therefore we switched on median recentering in `p3d_cobjex`. Compared to extractions where we experimentally turned off this feature, we saw a clear improvement in signal-to-noise, even though the determined offset was typically less than half a pixel. Cosmic-ray hit removal was implemented within `p3d_cobjex`, utilizing the `PyCosmic` (Husemann et al. 2012) algorithm. We also chose the option to subtract a scattered light model before extraction, as advised for PMAS LArr data (Sandin et al. 2012). Next, the `p3d_sensfunc` routine was utilized to create sensitivity functions. Here we first created a 1D standard star spectra with the `p3d_sensfunc` GUI using the extracted standard star observations. Then these sensitivity functions were applied to every extracted target exposure using the `p3d_fluxcal` task. For correction of atmospheric extinction we used values from the empirical Calar Alto extinction curve model (Sánchez et al. 2007).

The final data products resulting from the `p3d` pipeline are flux calibrated datacubes for all target exposures. `p3d` also produces the corresponding error cubes, containing the standard-deviation of each volume pixel ('voxel'). After trimming regions affected by vignetting on the detector (Roth et al. 2010), the cubes cover a wavelength range from 3600–4600 Å sampled on identical wavelength grids ($\Delta\lambda = 0.75 \text{ Å px}^{-1}$). Their spectral resolution, determined from fitting 1D Gaussian profiles to several lines in the spectra of the extracted arc-lamp frames, is $v_{FWHM} \approx 160 \text{ km s}^{-1}$ ($R \approx 1850$). We note there is a spatial and spectral dependence of R in PMAS (see also Sánchez et al. 2012, Sect. 6.2), and the value reported here is the median near the centrum of our wavelength range.

2.3. Sky subtraction

To remove night sky emission from the datacubes, we created for each target a median spectrum from the ring of spaxels bracketing the FoV (ignoring low-transmission fibres) and subtracted this from every spaxel. Even though the median is more robust against contamination of signal from the target than the mean, it is still possible that we subtracted a fraction of the nebular emission if this emission extended out into and beyond the FoV. However, we note that most of the known extended Ly α regions² around RQQs have projected maximum extents of $\lesssim 65 \text{ kpc}$, corresponding to $\lesssim 8''$ (the PMAS FoV) at the redshifts of our objects. Nevertheless, we first visually inspected all datacubes if any obvious extended emission features were present, and then checked the individual outer-ring median spectra if they contain spikes not attributable to sky lines. Both tests were negative, so we are certain at this point not having accidentally removed very

bright extended nebular emission. Nevertheless, we will return to this point in our analysis in Sect. 3.5, showing that for special cases of large-scale extended emission our observing strategy may have been less than optimal.

2.4. Stacking the individual exposures for each QSO

To increase the signal-to-noise of faint emission we stacked the individual sky-subtracted & flux-calibrated datacubes. During the observations the QSO was centered in the LArr FoV using the acquisition and guiding (A&G) system of PMAS. No dithering scheme was intended, to avoid cross-correlation of neighbouring spaxels on the sky. Unfortunately the filter wheel of the A&G camera was set to V-Band, causing the QSOs centroid point source to move around within our bluer wavelength range due to differential atmospheric refraction, even though the guide star observed with the A&G system remained steady. We corrected for these unintended dither offsets by spatial integer pixel shifts before stacking. Integer pixel shifts were preferred over fractional shifts to avoid interpolation effects and thus keeping the original observational information as unaffected as possible.

In practice, we first determined the QSOs centroid position in the individual exposures using images created from summing up datacube layers around $\lambda_{Ly\alpha}(z_{QSO})$. If a centroid was shifted more than a half pixel along a spatial axis, this cube was then shifted by a pixel along this axis in the opposite direction. No exposure needed to be shifted by more than one pixel in x or y direction. Because of the varying sky background (and different exposure times in the case of Q0256–0003) we employed a variance-weighted mean for stacking, using the error cubes generated by the pipeline.

Having reduced the raw data as described, we were now left with five datacubes containing voxels $F_{x,y,z}$, where (x,y) are the spatial indices, and z is the index for the spectral layers, in units of $10^{-17} \text{ erg s}^{-1} \text{ cm}^{-2} \text{ Å}$.

3. Analysis & results

3.1. QSO spectra

We show spectra of our five QSOs in Fig. 1. These spectra were extracted in a $3''$ diameter aperture centered on the highest S/N spectral pixel (spaxel). Where available, we overlay SDSS DR9 (Ahn et al. 2012) spectra. Our spectra differ to SDSS by $\lesssim 10 \%$ for Q0027+0103 & Q0308+0129; for UM 247 there is a systematically offset by $\lesssim 20 \%$ in the blue. Quasar variability, spectrophotometric uncertainties in the SDSS or imperfections in our flux calibration could be reasons for these differences. We note that for Q0308+0129 the observing conditions were not photometric, thus our fluxes of this object are likely somewhat too low.

² Using the compilation in Fig. 3 of Cantalupo et al. (2014) and 10 additional detections reported by Hennawi & Prochaska (2013).

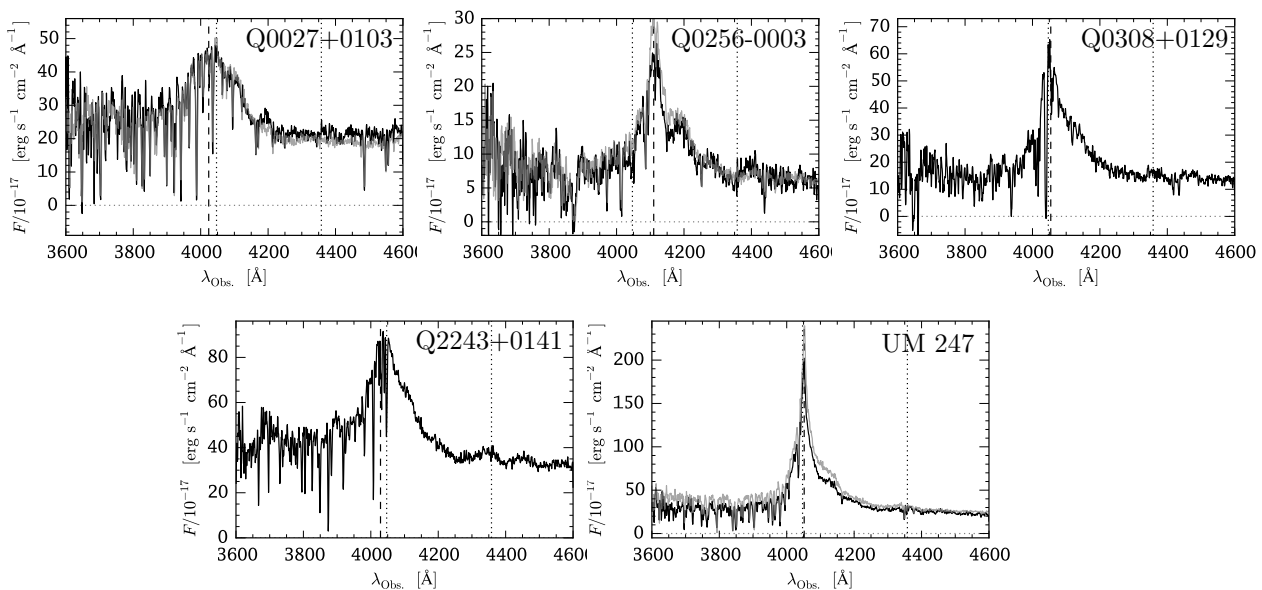


Fig. 1. Extracted spectra from the PMAS datacubes in a 3'' diameter aperture. For those objects where available (Q0027+0103, Q0256-0003 & UM 247) SDSS DR9 spectra have been over-plotted in grey to illustrate the quality of our flux calibration. The vertical dashed line shows the wavelength of Ly α at the QSOs redshift and the vertical dotted lines indicate the wavelengths of the artificial telluric Hg I (4047 Å & 4358 Å) emission-lines.

The night sky emission line spectrum in Calar Alto shows significant man-made contributions, arising from tropospheric scattering of high-pressure street lamps in nearby populated areas. In our wavelength range the Hg I 4047 Å & 4358 Å emission lines are prominent. Wavelengths of these lines and the expected Ly α wavelength $\lambda_{\text{Ly}\alpha}^{\text{Obs.}} = (1+z_{\text{QSO}}) \cdot \lambda_{\text{Ly}\alpha}$ are indicated in Fig. 1. As can be seen, the λ_{4047} line is located unfavorably close near the expected peak of the Ly α emission for 4 of our QSOs. We had not anticipated the strength of this anthropic line in the planning of our observations. This unresolved line has an average surface brightness of $F_{4047}^{\text{Hg I}} = 3.5 \times 10^{-16} \text{ erg s}^{-1} \text{ cm}^{-2} \text{ arcsec}^{-2}$ (Sánchez et al. 2007) and thus, by amplifying the background noise in a narrow-band window around $\lambda_{\text{Ly}\alpha}^{\text{Obs.}}$, contributes negatively to our efforts in uncovering extended Ly α emission. The sensitivity in this narrow-band is further decreased by residuals from sky subtraction, resulting from the varying spectral resolution across the FoV (Sect. 2.2).

3.2. Subtraction of QSO emission from the datacubes

Due to the PSF broadening, spectra at radial distances $\lesssim 2''$ from the QSO center are visibly contaminated by the nuclear spectrum. Thus, in order to reveal possible extended Ly α emission around the QSO, we had to remove this contamination. CJW06 experimented with three algorithms to achieve this *deblending* in PMAS LArr datacubes:

- *On- minus scaled off-band method*: An on- and off-band image is created from the datacube. The latter is then scaled and subtracted from the former, thereby revealing possible contribution of extended emission in the on-band. Here the *on-band* is obtained as a summation in wavelength direction over all datacube layers expected to contain the extended-emission signal, while the *off-band* is a sum over nearby layers not being affected by extended emission. Asserting that the extended emission contributes only a few percent to the on-bands peak intensity (i.e. QSO+extended emission), the

ratio between the peak intensities in on- and off-band is a sufficient scale factor for the subtraction.

- *Analytical PSF Extraction*: An analytical PSF model is fitted and subtracted from every datacube layer, thereby creating a datacube which should only contain non-nuclear emission. Then an iterative scheme is employed, where in a second iteration positional and shape parameters of the PSF function are fixed, using values from the first iteration with the constraint of allowing them to vary only smoothly with wavelength (see e.g. Wisotzki et al. 2003; Kamann et al. 2013, for more elaborate versions of this technique involving multiple point-sources within the FOV). According to CJW06 the analytical PSF extraction produces unsatisfying results in PMAS in terms of QSO residuals, so we did not consider applying this method to our data.
- *Empirical PSF Subtraction*: By summation over datacube layers expected to be unaffected by extended emission, an empirical PSF image is created. It is then scaled and subtracted from every layer, thus creating a residual datacube containing extended emission. To find the scaling the PSF image with respect to the datacube layers, a spectrum is aperture-extracted from the datacube, with every spaxel in the aperture having weights assigned via the PSF image. An iterative scheme is employed to remove contamination in the scaling spectrum from extended emission possibly covering parts of the aperture: the datacube resulting from the deblending is subtracted from the undeblended datacube from which in turn the next scaling spectrum is extracted. A variant of this method was developed by Husemann et al. (2013), where in subsequent iterations the correction is achieved using an annulus-extracted spectrum from the deblended datacube.

We emphasize the methodological similarity between the *on- minus scaled off-band method* and the *empirical PSF subtraction* deblending: If the PSF image in the latter is created from the same layers as the off-band in the former, every layer in the

deblended datacube can be thought of as an ‘on-band’ having a scaled ‘off-band’ subtracted. If, moreover, no iterative corrections are applied, the image resulting from the *on- minus scaled off-band method* is identical to the image resulting from summation over the on-band defining layers in the empirical PSF subtracted datacube. Note that the iterative correction only increases the fidelity of an extended emission signal when it is measurably present after the first deblending iteration; otherwise only noise is shuffled around in subsequent iterations.

Because of this similarity we applied solely the *empirical PSF subtraction* method to our datacubes. As PSF image we take ~ 40 layers ($\sim 30 \text{ \AA}$) beginning $\sim 10 \text{ \AA}$ redwards of $\lambda_{\text{Ly}\alpha}(z_{\text{QSO}})$. We found this choice to produce the best results in terms of subtraction residuals, because of the following reasons: Firstly, for the red side of $\lambda_{\text{Ly}\alpha}(z_{\text{QSO}})$, a redward band gives a better signal-to-noise ratio for the PSF image due to $z_{\text{abs}} \approx z_{\text{em}}$ Ly α absorbers appearing blueward of $\lambda_{\text{Ly}\alpha}(z_{\text{QSO}})$ (see Fig. 1). Secondly, as we did not correct for differential atmospheric refraction, the position and shape of the PSF changes with λ , thus selecting layers further away would produce a non-optimal representation of the PSF at the expected position of Ly α fuzz, resulting in stronger residuals from the subtraction ($\lambda_{\text{Ly}\alpha}(z_{\text{QSO}})$). This is also the reason why we chose the spectral window to be relatively narrow.

We experimented with different extraction apertures for the scaling spectrum. Visual inspection revealed no extended emission after the first iteration in all objects. As expected (see above), performing more iterations does not improve upon this. We thus decided to use the smallest possible aperture for scaling, i.e. the single spaxel with the highest S/N. Despite this, we could not find any evidence for extended Ly α fuzz around any of our targets, except a small-scale feature to the north of UM 247.

To visualize our findings, we show in Fig. 3 narrow-band images centered on $\lambda_{\text{Ly}\alpha}(z_{\text{QSO}})$ created by summing over 20 layers (15 \AA) of the residual datacubes. Instead of using physical units, the scale on the colour bar uses multiples of the standard-deviation per pixel. This colour bar scaling simplifies the judgment whether features seen in this image are actually significant, and it also makes the comparison between the panels straightforward. Except for UM 247, none of these images shows any significant feature.

In Fig. 2 we show spectra from the residual datacubes extracted within a small circular aperture consisting of 20 spaxels (aperture with outer radius $r_C = 1.25''$, cf. Sect. 3.3) centered around the scaling spectrum. Again, only UM 247 displays a distinct spectral line that seems inconsistent with noise. We discuss this feature further in Sect. 4.2.

3.3. Estimation of detection limits

From our visual inspection of the residual datacubes (see also Figs. 3 & 2) we conclude that in 4 out of 5 objects we have no significant detections. We now want to constrain an upper limit in surface brightness for extended Ly α nebulae around those QSOs. To do so, we define confidence limits for rejecting the null hypothesis, which states that there is no extended Ly α emission present in the data. The upper limit is then given as the minimum surface brightness for which we would not be able to confidently reject the null hypothesis anymore.

We adopted circular apertures centered on the scaling spectrum. In absence of morphological information for the non-detections, this simplification appears reasonable, although it is known that QSO CGM Ly α nebulae can be asymmetric (e.g. Weidinger et al. 2004; Rauch et al. 2013). For such nebulae the

average surface brightness within a circular aperture will generally be lower than a surface brightness obtained within an isophote.

We explored successively larger apertures around the central scaling spectrum by adding annuli with a width of one pixel. This defined 8 ‘circular’ apertures C_k ($k = 1 \dots 8$) with outer radii of $r_C = (2k + 1)/4''$. The numbers of spaxels N_C in those apertures are then $N_{C_k} = (8, 20, 36, 68, 96, 136, 176)$.

The assessment was performed on the residual datacube $F'_{x,y,z}$ after PSF subtraction. The residual signal S_k within the relevant spectral layers and inside each circular aperture C_k can be written as

$$S_k = \sum_{(x,y) \in C_k} I_{x,y}, \quad (1)$$

where $I_{x,y} = \sum_{z \in \text{NB}} F'_{x,y,z}$ is the value of a pixel in the narrow-band images shown in Fig. 3. For the sake of brevity, we do not explicitly state units and conversions in our equations.

Assuming for the moment that we had reliable variance estimates $\sigma_{x,y}^2$ for every pixel of the pseudo narrow-band image $I_{x,y}$ (or equivalently $\sigma_{x,y,z}^2$ for every voxel of the residual datacube), the noise in C_k could be written as

$$\sigma_k = \frac{1}{N_{C_k}} \sqrt{\sum_{(x,y) \in C_k} \sigma_{x,y}^2}, \quad (2)$$

Combining now Eqs. (1) and (2), we could express the signal S_k within C_k in amounts of the noise σ_k being present in C_k , i.e.

$$S_k = n \cdot \sigma_k, \quad (3)$$

where, under assumption of pure Gaussian noise, n would directly translate into a probability of the null hypothesis – no nebular emission detected – being false (e.g. Wall 1979).

However, neither of the above made assumptions – having reliable variance estimates for every voxel and pure Gaussian noise – are met by our data: The QSO subtraction introduces non-Gaussian residuals, as does the background subtraction (Sect. 2.3), which are not captured by the formal variances. There may also be further unknown systematics. We therefore replaced the formal variances by two empirical proxies for $\sigma_{x,y}$:

- $\bar{\sigma}_k^{\text{spat}}$: The standard deviation (relative to an expectation value of zero) per pixel of the narrow-band image $I_{x,y}$ outside of the circular aperture C_k .
- $\bar{\sigma}_k^{\text{spec}}$: The standard deviation (relative to an expectation value of zero) per spaxel within the circular aperture C_k , calculated from spectral layers not contributing to the narrow-band images. The calculation is limited to wavelengths not further than 75 \AA away from $\lambda(z_{\text{QSO}})$, since here the empirical PSF subtraction starts to produce strong residuals because of differential atmospheric refraction.

Note that both noise estimators depend on the aperture C_k .

With these proxies we then set $\sigma_{x,y} \approx \bar{\sigma}_k^{\text{spat}}$ or $\sigma_{x,y} \approx \bar{\sigma}_k^{\text{spec}}$ for all x, y in Eq. (2) and obtain

$$S_k = n_{\text{spat}} \cdot (\bar{\sigma}_k^{\text{spat}} / \sqrt{N_{C_k}}), \quad (4)$$

$$S_k = n_{\text{spec}} \cdot (\bar{\sigma}_k^{\text{spec}} / \sqrt{N_{C_k}}). \quad (5)$$

We show below that $n_{\text{spec}} \approx n_{\text{spat}}$ (or equivalently $\bar{\sigma}_k^{\text{spec}} \approx \bar{\sigma}_k^{\text{spat}}$) holds.

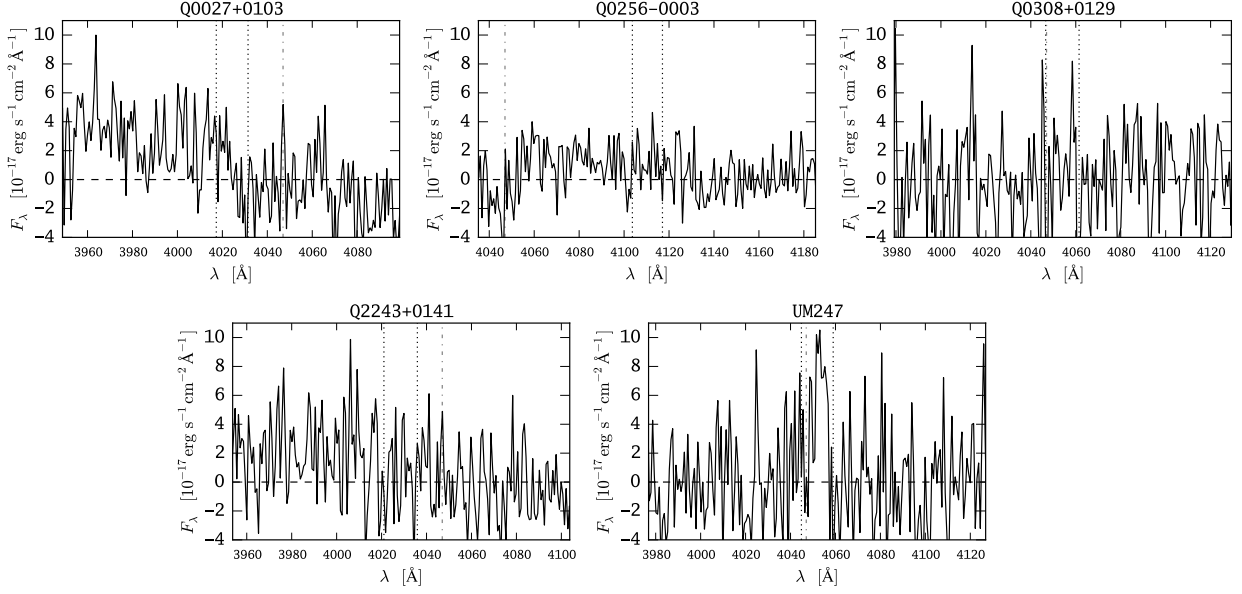


Fig. 2. Residual spectra for our 5 QSOs from the QSO-subtracted datacubes, extracted within the $r_c = 1.25''$ aperture (cf. Sect. 3.3) around the scaling spectrum. The *vertical dotted lines* indicate the boundaries of the narrow-band image ($15 \text{ \AA} = 20$ layers), shown in Fig. 3. The *vertical dashed-dotted lines* show the position of the Hg I-sky line (Sect. 3.1).

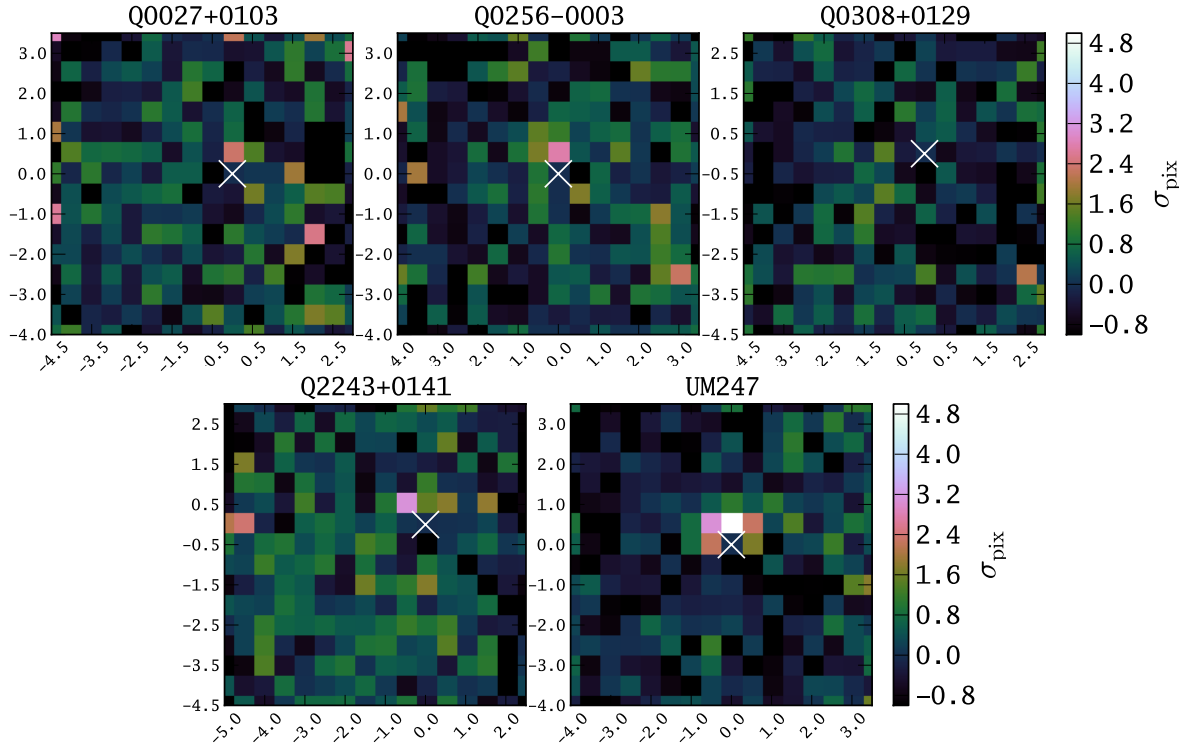


Fig. 3. Narrow-band images (15 \AA wide, centered on $\lambda_{Ly\alpha}(z_{QSO})$) for our 5 QSOs. These images were created from the QSO-subtracted datacubes using the empirical PSF subtraction method. The position of the spaxel used for scaling the PSF image is indicated by a cross; this position corresponds to the centroid of the QSO nucleus. Colours indicate multiples of the standard-deviation per pixel σ_{pix} , calculated for each image. The values of σ_{pix} are $(2.3, 1.4, 2.7, 2.6, 3.5) \times 10^{-17} \text{ erg s}^{-1} \text{ cm}^{-2}$, from top left to bottom right. North is up, and East is to the left. Axes ticks are $\Delta\delta$ and $\Delta\alpha$ in arcseconds with respect to the QSO centroid.

The question is, which n_{spec} or n_{spat} is required, in each QSO, for a detection? We addressed this problem by adding simulated extended emission into our datacubes before subtracting the QSO. Specifically we used circular nebulae of an extent that would fill a particular aperture C_k . These simulated nebulae had

a flat surface brightness profile and a Gaussian line profile with 300 km s^{-1} FWHM (approximately twice the spectral resolution) centered around $\lambda_{Ly\alpha}(z_{QSO})$. We emulated seeing effects by convolving those nebulae with 2D Gaussians of the average seeing FWHM of the particular observation. Using the above defined

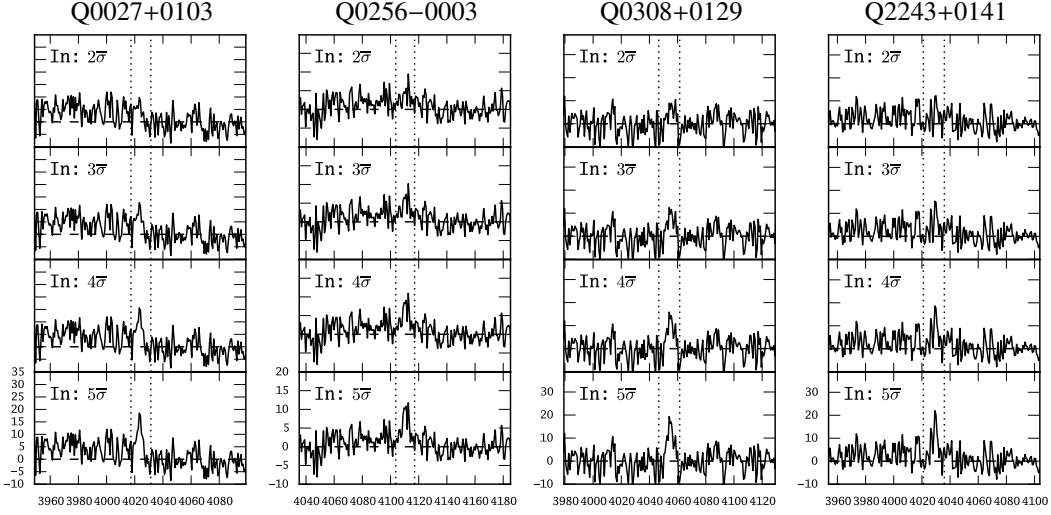


Fig. 4. Examples of recovered spectra after adding artificial nebulae into the datacube prior to the empirical PSF subtraction. The surface brightness of the artificial nebulae was scaled with integer values of n_{spat} according to Eq. (4). After empirical PSF subtraction the spectrum was extracted from the residual datacube using the $r_C = 1.25''$ aperture (i.e. the same as in Fig. 2). The spectra are shown in units of $10^{-17} \text{ erg s}^{-1} \text{ cm}^{-2} \text{ \AA}^{-1}$. Note that artificial nebulae with $n_{\text{spat}} \geq 5$ can be unambiguously discriminated from the background for all objects.

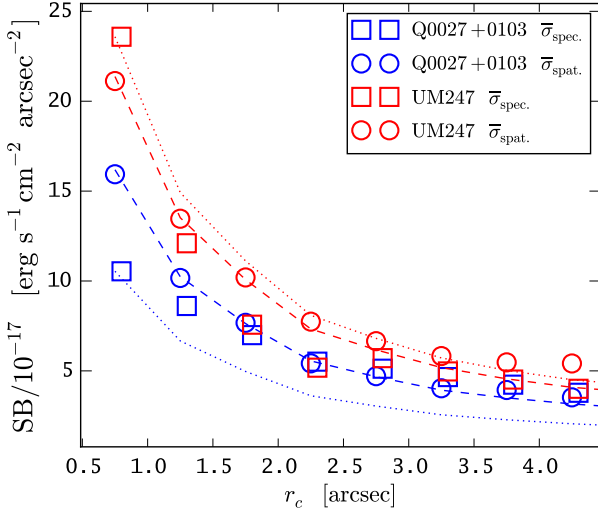


Fig. 5. Comparison of formal 5σ surface brightness detection limits as a function of aperture radius using the different noise estimators $\bar{\sigma}_{\text{spat}}$ and $\bar{\sigma}_{\text{spec}}$, exemplarily shown for two objects (Q0027+0103 - blue symbols, UM 247 - red symbols panel). The agreement between $\bar{\sigma}_{\text{spat}}$ and $\bar{\sigma}_{\text{spec}}$ is similarly good for the other objects.

noise proxies we scaled the surface brightness of the nebulae by integer multiples n_{spat} according to Eq. (4). We downsampled our simulated nebulae to the grid of our datacubes and added them before the final step of empirical PSF subtraction. By visual inspection of the residual cubes we found that nebulae with $n_{\text{spat}} = 5$ can be unambiguously discriminated from the background. Exemplarily we show in Fig. 4 the results of this numerical experiment for nebulae covering the $r_C = 1.25''$ aperture. Results for other aperture sizes were similar, i.e. a $5\bar{\sigma}_{\text{spat}}$ input according to Eq. (4) yielded an unambiguous visual detection after PSF subtraction.

We now demonstrate that both noise proxies yield similar results for our surface brightness limits, defined as the minimum surface brightness that a circular nebulae with a particular radius could have before it would fall below our detection criterion.

For this purpose we show in Fig. 5 the surface brightness limits exemplarily for two objects, as a function of aperture radius. These limits were calculated using either Eq. (4) or Eq. (5) with $n_{\text{spat}} = 5$ or $n_{\text{spec}} = 5$. Figure 5 shows the trend expected for a noise estimate independent of aperture, obtained by scaling the curve for the smallest aperture ($r_C = 0.75''$) by aperture area $\propto N_{C_k}^{-1/2}$. Note that indeed $\bar{\sigma}_{\text{spec}}$ and $\bar{\sigma}_{\text{spat}}$ have similar values, and that there is only a mild dependence on aperture size. For the cases not shown, the agreement is similar. Since also no a priori distinction can be made as to which of the two proxies is better, we quote the average $(\bar{\sigma}_{\text{spec}} + \bar{\sigma}_{\text{spat}})/2$ as our detection limits in surface brightness.

3.4. Surface brightness limits on extended emission

The resulting surface brightness upper limits for extended Ly α emission surrounding the observed QSOs, calculated by applying the method presented in the previous section, are shown in Fig. 6. For reference, the obtained upper limits for Ly α fuzz with $2.5''$ (20.5 kpc) radial extend – the typical extent of circum-QSO Ly α fuzz predicted by Haiman & Rees (2001) – are $(5.4, 3.4, 6.5, 6.0, 6.3) \times 10^{-17} \text{ erg s}^{-1} \text{ cm}^{-2} \text{ arcsec}^{-2}$ for the quasars Q0027+0103, Q0256-0003, Q0308+0129, Q2243+0141, and UM 247, respectively.

In Fig. 6 we also show the integrated signal with a circular aperture, i.e. Eq. (1) transformed to surface brightness units. Here the error bar on the integrated signal indicates the standard deviation within the aperture. In our case, this is a measure for how asymmetric possible signal is distributed within the aperture; e.g. for UM 247, a bright spot appears only to the north of the object, thus the error bar on the integrated signal within the circular aperture is large. Note that for all objects except UM 247 the integrated signal is always below our detection limits, thus confirming the visual impression gained from Figs. 3 and 2. We discuss the fuzz around UM 247 further in Sect. 4.2.

Background offsets, positive or negative, can be seen in the integrated signal for Q0308+0129 or Q2243+0141 – however, note that we incorporated these systematics in the calculation of our detection significances by forcing the expectation value to

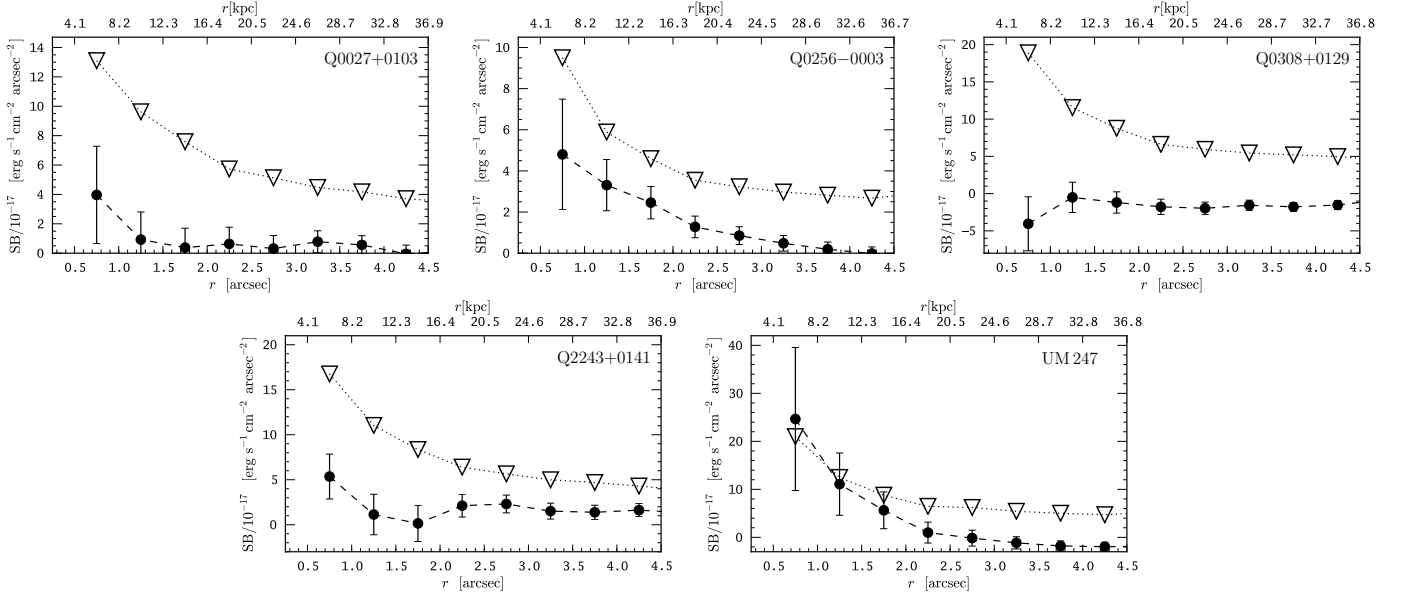


Fig. 6. Surface brightness upper limits (triangles) for circularly symmetric extended Ly α emission around our 5 QSOs as a function of radial angular (bottom abscissa) or physical extent (top abscissa). The integrated observed signal within each apertures is shown by the black points, where the error bars indicates the standard deviation within the aperture, as a measure of the irregularity of the flux distribution within the aperture.

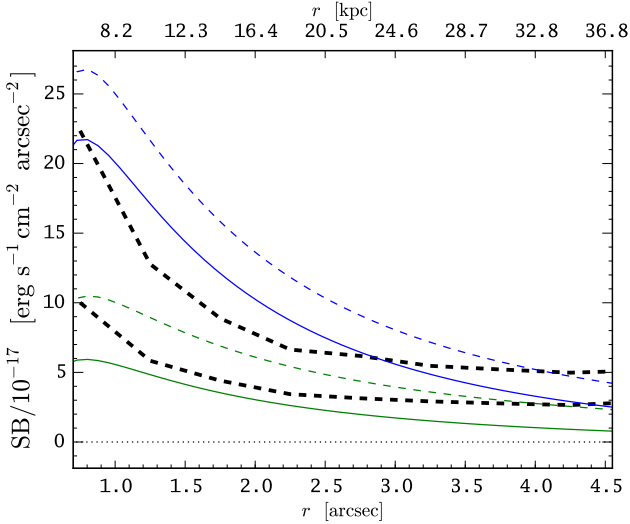


Fig. 7. Expected average surface brightness profiles for exponential nebulae $SB_{Ly\alpha}(r) = \Sigma_0 \times \exp(-r/r_0)$, measured within circular apertures and compared to our surface brightness upper limits (dashed lines, indicating the range of our limits shown in Fig. 6). Coloured solid lines show the expectations including the effect of our sky subtraction procedure, while the dashed lines ignore it (blue: $\Sigma_0 \approx 10^{-16} \text{ erg s}^{-1} \text{ cm}^{-2} \text{ arcsec}^{-2}$ and $r_0 = 2''$; green: $\Sigma_0 = 5 \times 10^{-17} \text{ erg s}^{-1} \text{ cm}^{-2} \text{ arcsec}^{-2}$ and $r_0 = 4''$).

zero for our noise proxies (see above). There also appears a hint of possible extended emission in Q0256-0003, which is however below our detection threshold and not confidently separable from noise in the residual datacube.

3.5. Effect of sky subtraction on large-scale Ly α fuzz.

Recently, two nebulae were discovered that have sizes significantly larger than our field of view (Cantalupo et al. 2014; Martin et al. 2014a, see Table 2). As explained in Sect. 2.3, we subtracted a median spectrum generated from the outer spax-

els framing our field of view to remove emission by the night sky. Would giant nebulae as the above mentioned still leave a detectable signal in our observations?

From the intensity map presented in Cantalupo et al. (2014) we see that at a distance of $r \approx 5''$ to the QSO UM 287, their nebula has a mean surface brightness of $\approx 5 \times 10^{-17} \text{ erg s}^{-1} \text{ cm}^{-2} \text{ arcsec}^{-2}$. At a similar distance to their central QSO, Martin et al. (2014a) measured a surface brightness of $\approx 9 \times 10^{-18} \text{ erg s}^{-1} \text{ cm}^{-2} \text{ arcsec}^{-2}$. If the surface brightness profile increases towards the center, the central parts might still leave a significant detectable signal in our datacubes. If, however, the central surface brightness profile is rather flat, the significance of the recoverable signal will be substantially reduced. Unfortunately, currently no information on the central parts of the surface brightness profile in UM 287 is available (Cantalupo, priv. comm.).

We investigated the recoverability of the nebula in UM 287 assuming two different exponential surface brightness profiles, $SB_{Ly\alpha}(r) = \Sigma_0 \times \exp(-r/r_0)$ with $r_0 = 2''$ and $r_0 = 4''$, which are fixed to UM287's surface brightness of $10^{-17} \text{ erg s}^{-1} \text{ cm}^{-2} \text{ arcsec}^{-2}$ at $r = 5''$. The central surface brightness of the $r_0 = 2''$ profile is then $\Sigma_0 \approx 10^{-16} \text{ erg s}^{-1} \text{ cm}^{-2} \text{ arcsec}^{-2}$ and for the $r_0 = 4''$ profile $\Sigma_0 = 5 \times 10^{-17} \text{ erg s}^{-1} \text{ cm}^{-2} \text{ arcsec}^{-2}$. Our sky subtraction procedure would subtract a constant surface brightness of $SB(4'') \approx 1.5 \times 10^{-17}$ from both profiles. We note that such a faint signal would not have been seen in the visual inspection of the subtracted sky spectra.

Applying our detection criterion in Fig. 7, the $r_0 = 2''$ profile would still permit a significant detection of the nebula. However, for the flatter $r_0 = 4''$ profile the recovered signal would fall below the detection threshold. And obviously we would always underestimate the true extent of the nebula. We emphasize that our observations were originally not designed with such large scale nebulae in mind and their recent discovery came as a surprise.

Table 2. Compilation of observational results from the literature on extended Ly α emission around radio-quiet QSOs (single-object investigations).

| Reference | Quasar | Redshift | Extent | Flux | Method |
|----------------------------|------------------|----------|-----------------------|-----------------------|-----------------------------|
| Bergeron et al. (1999) | Q 2233-606 | 2.238 | $9.2'' \times 12.1''$ | 3.2×10^{-15} | narrow-band imaging |
| Bunker et al. (2003) | PC 0953+4749 | 4.46 | $\approx 5''$ | 3.6×10^{-17} | long-slit spectrum |
| Weidinger et al. (2005) | Q 1205-30 | 3.041 | $\approx 10''$ | 7×10^{-16} | narrow-band & long-slit |
| Francis & McDonnell (2006) | PSS 2155+1358 | 4.28 | $\leq 0.7''$ | 1.7×10^{-17} | integral field spectroscopy |
| Goto et al. (2012) | CFHQS J2329-0301 | 6.417 | $\sim 1.3 - 1.5''$ | 8×10^{-17} | long-slit spectrum |
| Rauch et al. (2013) | Q J0332-2751 | 3.045 | $2.2''$ | 5.4×10^{-17} | long-slit spectrum |
| Cantalupo et al. (2014) | UM 287 | 2.28 | $\approx 55''$ | 5.5×10^{-15} | narrow-band imaging |
| Martin et al. (2014a) | HS 1449+19 | 2.843 | $\geq 30''$ | 2.0×10^{-13} | integral-field spectroscopy |

Notes. Flux is given in $\text{erg s}^{-1} \text{cm}^{-2}$. Measurements on the fuzz around CFHQS J2329-0301 have also been published by Willott et al. (2011), who obtained similar results. No flux has been reported by Bunker et al. (2003) for the flux of the extended Ly α emission surrounding PC 0953+4749, but this object is also part of the CJW06 sample. The flux for the nebula around HS 1449+19 is from Table 3 in Martin et al. (2014a). See text for possible caveats considering the comparability of the presented values on flux and extent.

Table 3. Compilation of observational results from the literature on extended Ly α emission around radio-quiet QSOs (samples).

| Reference | Radio-Quiet Quasars | | Redshift | SB limit | Instrument - Method |
|------------------------------------|---------------------|---------------|-------------------------------|----------------------------|------------------------------------|
| | Targeted | Fuzz detected | | | |
| CJW06 ^(a) | 6 | 4 | $2.7 \lesssim z \lesssim 4.5$ | $\sim 10^{-17}$ | PMAS – integral-field spectroscopy |
| North et al. (2012) ^(b) | 6 | 4 | $z \sim 4.5$ | $\sim 5 \times 10^{-19}$ | FORS2 - slit spectroscopy |
| Hennawi & Prochaska (2013) | 29 | 11 | $z \sim 2$ | $\sim 5 \times 10^{-18}$ | LRIS & GMOS - slit spectroscopy |
| This study | 5 | 1 | $z \sim 2.3$ | $\sim 5.5 \times 10^{-17}$ | PMAS – integral-field spectroscopy |

Notes. (a) Surface brightness limit for CJW06 estimated by us. (b) North et al. (2012) is an extension of Courbin et al. (2008). Surface brightness limit in $\text{erg s}^{-1} \text{cm}^{-2} \text{arcsec}^{-2}$.

4. Discussion

4.1. Comparison with observations from the literature

How do our upper limits in surface brightness for extended Ly α emission around radio-quiet QSOs compare with previous investigations of this phenomenon? Most of the studies reporting a successful attempt in detecting circum-QSO Ly α fuzz (sometimes serendipitous discoveries) have focused on single objects. We compiled a list of such investigations in Table 2. Beyond these single-object results, very few studies aimed at constructing actual samples (which were always small). We list the relevant publications in Table 3.

Substantial methodological differences between the studies listed in Tables 2 & 3 have to be kept in mind when comparing those results with our non-detections. The sizes in Table 2 often refer to the maximum extent at which the authors were able to detect Ly α emission. This quantity obviously depends on the depth of the observations and, in the case of long-slit spectroscopy, the orientation of the slit. For the latter case, fluxes are also affected by significant slit-losses, since only a fraction of the nebula is usually captured. Finally, line emission from the central QSO might contaminate the fluxes of the nebular component in some cases, especially since a subtraction of the QSO point source was not performed in some cases (e.g. Bergeron et al. 1999; Martin et al. 2014a; Rauch et al. 2013).

The quoted values for the surface brightness limits of the samples in Table 3 are also very rough estimates, as the actual limits depends on the assumed size of the fuzz (see our derivation in Sect. 3.3 and also the derivation in Sect. 4.3 of Hennawi & Prochaska 2013) and, moreover, they differ from target to target due to differences in the used instruments and observing strategies. Unfortunately, CJW06 did not quantify the depth of their observations. Since they also used PMAS (although in

a different setup than we) and knowing the typical instrumental and atmospheric parameters, we estimated that their detection sensitivity was similar to that in our study.

We next considered whether the Ly α fuzz detected by the studies listed in Tables 2 and 3 would have been recovered if ‘implanted’ into our quasars. For this exercise we selected only objects for which the reported maximum extent (after de-redshifting) would be covered by our field of view. The Martin et al. (2014a), Cantalupo et al. (2014) and Bergeron et al. (1999) objects do not fulfill this criterion (see also Sect. 3.5). We also excluded the Rauch et al. (2013) object, since their flux value is contaminated by quasar Ly α emission. We then circularized the nebulae, i.e. we assumed the flux to be distributed symmetrically around the quasar with a radius defined as half the maximum extent. After calculating de-redshifted radii and surface brightness levels, we determined the integrated signals within circular apertures covering the whole nebulae. Note that only Weidinger et al. (2005) provided a surface brightness profile, so that only for this object we could calculate the integrated signal at various radii.

In Fig. 8 we plot the results from this exercise and compare them to our surface brightness limits: Out of 11 nebula used in this calculation, 3 would be detected in all our observations, further 4 would yield a 5σ detection only in our deepest dataset, and 4 would not be recoverable at all. (Note however that the circularization is actually reducing the signal from sources that have significantly asymmetric flux distributions. Thus a nebula yielding a 5σ detection only in our deepest dataset might have been recovered at a higher significance if the area over which the signal was integrated was better matched to the light distribution of the nebula.)

Note that half of the points in Fig 8 are at radii less than 10 kpc and 8 out of 10 are below 25 kpc. Small scale Ly α fuzz appears to be quiet frequent around radio-quiet QSOs. This is

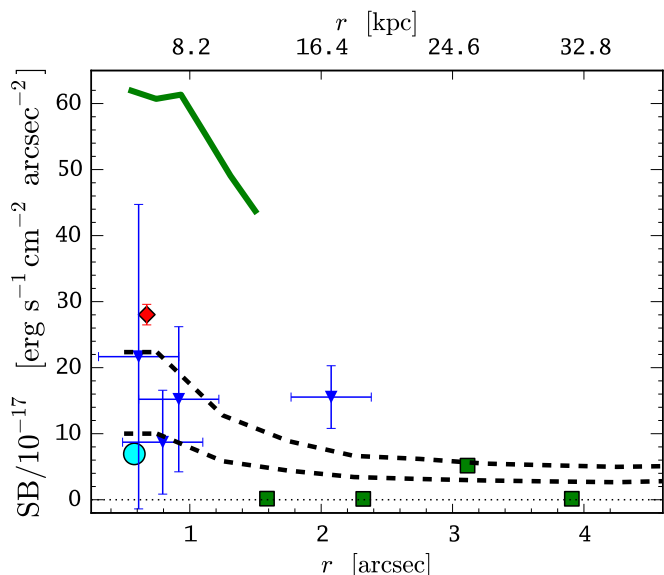


Fig. 8. Comparison of our surface brightness upper limits as a function of radius (thick dashed lines) to the reported literature detections of circum-QSO Ly α emission, de-redshifted to $z = 2.3$, and assuming that the reported maximum extent defines the radius of the detection aperture. The symbols feature results from the CJW06 sample (*blue triangles* with error bars), from the North et al. (2012) sample (*green squares*), the nebula from Goto et al. (2012) (*red diamond*) and the fuzz from Francis & McDonnell (2006) (*cyan circle*). We also show the integrated signal at various radii from the de-redshifted Weidinger et al. (2005) surface brightness profile (*solid green line*).

also supported by the high recovery rate of this phenomenon in Hennawi & Prochaska (2013), although their detections are generally fainter. We argue in the next section that the signal we find around UM 247 also falls into this category.

Finally, we point out that most of the reported detections of bright Ly α fuzz are typically at $z \gtrsim 3$. Our recovery rate of this phenomenon at $z \approx 2.3$ (20%) is lower compared to CJW06 (66%). Moreover, Hennawi & Prochaska (2013) report a recovery rate of 38% at $z \sim 2$. Observations are insufficient at this stage to infer a redshift evolution of circum-QSO Ly α fuzz properties. It is nevertheless intriguing that Zirm et al. (2009) find that Ly α nebulae enshrouding radio-loud QSOs decline in size and luminosity with decreasing redshift. If real, such a decline could indicate a depletion of the cool gas content of the CGM (at least on average). Extending such a trend to radio-quiet QSOs would however require much larger and more homogenous samples over a range of redshifts.

4.2. Small-scale Ly α fuzz near UM 247

UM 247 is the only object in our sample with a formally significant residual at Ly α after PSF subtraction. To assess whether this residual is real and not an artefact caused by a fault (e.g. an undetected cosmic) in a single exposure, we repeated the stacking of the individual exposures (Sect. 2.4) 5 times, each time with one exposure excluded from the stack. We then performed the empirical PSF subtraction in exactly the same manner as described above (Sect. 3.2) for each of those stacks. The feature remained, hence we assert that it is genuine.

This basically unresolved excess emission is located at a distance of $d \lesssim 4$ –8 kpc (0.5–1'') north of UM 247. The line has a

flux of $\sim 5.6 \times 10^{-16}$ erg s $^{-1}$ cm $^{-2}$, corresponding to a Ly α luminosity of $L_{\text{Ly}\alpha} \approx 2.4 \times 10^{43}$ erg s $^{-1}$.

If the Ly α emission of this feature was powered purely by star formation, ignoring ionization of the nearby quasar as well as radiative transfer effects, this would correspond to a star formation rate of ~ 10 –20 M $_{\odot}$ yr $^{-1}$ (with the exact value being dependent on the metallicity of the underlying stellar population, see Schaerer 2003). This Ly α luminosity is the bright end of the Ly α emitter luminosity function for $z \sim 2.3$ (Blanc et al. 2011). Given the small field of view of our observations, the detection of such a bright Ly α emitter in close vicinity to a quasar would appear rather coincidental.

In an opposing scenario we consider the possibility that the Ly α radiation is produced purely by fluorescence of a compact nearby cloud, devoid of internal star formation and optically thick to ionizing radiation from the quasar. This cloud will behave as a special mirror, converting $\sim 66\%$ of all impinging hydrogen-ionizing photons into Ly α . Thus, given the quasar ionizing luminosity and the size of the cloud one can predict its Ly α luminosity (e.g. Francis & Bland-Hawthorn 2004; Adelberger et al. 2006; Kollmeier et al. 2010; Hennawi & Prochaska 2013). Since the cloud is unresolved, we adopt as an upper limit of its size the extent of one PMAS spaxel. Thus the physical surface extent of the Ly α emitting cloud is $R_{\text{cloud}}^2 \lesssim 16$ kpc 2 . From a measured QSO flux density of $f_{\lambda} = 2.5 \times 10^{-16}$ erg s $^{-1}$ cm $^{-2}$ Å $^{-1}$ for UM 247 at 4500 Å, we estimate a quasar luminosity at the Lyman edge of $L_{\nu_{\text{LL}}} = 8.0 \times 10^{29}$ erg s $^{-1}$ Hz $^{-1}$, assuming a power-law index of $\alpha_1 = 0.44$ ($f_{\nu} \propto \nu^{-\alpha}$) for the quasar continuum redward of the Lyman edge (Vanden Berk et al. 2001), and $\alpha_2 = 1.57$ blueward of 912 Å (Telfer et al. 2002). We also corrected for galactic extinction ($A_{\lambda} = 0.08$ at 4500 Å for UM 247), although that is a small effect. Assuming isotropic radiation, this results in an ionizing photon number flux of $\Phi = 4 \times 10^{10}$ s $^{-1}$ cm $^{-2}$ (1×10^{10} s $^{-1}$ cm $^{-2}$) at a distance of $d = 4$ kpc (8 kpc). The expected Ly α luminosity of a spherical cloud at this location follows as

$$L_{\text{Ly}\alpha} = 4\pi \times f_{\text{gm}} \times \eta_{\text{thick}} \times h\nu_{\text{Ly}\alpha} \times R_{\text{cloud}}^2 \times \Phi, \quad (6)$$

where η_{thick} is the fraction of ionizing continuum photons converted to Ly α photons, i.e. $\eta_{\text{thick}} = 0.66$. With f_{gm} we denote the geometric reduction factor – a free parameter that accounts for the inhomogeneous illumination of the cloud and subsequent redistribution of Ly α photons over a wide solid angle. Radiative transfer simulations suggest that for a transversely illuminated cloud $f_{\text{gm}} = 0.5$ (Kollmeier et al. 2010). For our upper limit on the cloud radius, Equation (6) then provides an upper limit on its Ly α luminosity of $L_{\text{Ly}\alpha} \lesssim 4 \times 10^{44}$ erg s $^{-1}$ (1×10^{44} erg s $^{-1}$) at $d = 4$ kpc (8 kpc). This is almost an order of magnitude higher than the observed value. In reality, however, the cloud size might be much smaller than our instrumentally imposed upper limit, and it might also be further away than the projected transverse distance. Hence this order of magnitude estimate of Ly α radiation emanating from the surface of an optically thick cloud in the vicinity of the quasar is still consistent with what we observe.

4.3. Comparison with models

Haiman & Rees (2001) presented a strongly idealized model to predict the luminosity of Ly α fuzz around radio-quiet quasars. Specifically, they assumed a spherical symmetric 2-phase gas distribution in pressure equilibrium within a collapsed dark-matter halo and predicted extended Ly α emission as a generic

property of high- z QSOs. The phases are a hot tenuous virialized plasma (i.e. $T_{\text{hot}} \sim T_{\text{vir}}$ of the halo) and colder neutral gas that has cooled down to $T_{\text{cold}} \sim 10^4$ K during the age of the system. If in such an environment the quasar emits radiation isotropically and ionizes the whole nebula, its Ly α luminosity depends only on the total gas mass and thus on the total halo mass. In this framework, the absence of significant Ly α fuzz in our QSOs might suggest that the hosting haloes are not overly massive. However, as already pointed out by Haiman & Rees (2001) and also Alam & Miralda-Escudé (2002), small deviations from this idealized scenario might alter the surface brightness of the Ly α fuzz substantially. Currently, the observations do not provide strong constraints on the basic assumptions in these models.

State-of-the-art numerical simulations in a cosmological framework predict that the spatial distribution of the CGM gas shows filamentary structure, with cold gas accreting along streams towards the center of the halo (e.g. Dekel et al. 2009; Faucher-Giguère & Kereš 2011; Rosdahl & Blaizot 2012). Those streams have high column densities and their surfaces will therefore reflect up to 2/3 of incoming ionizing photons as Ly α photons. Although Ly α cooling radiation from those streams alone might already produce a detectable signal in extremely massive haloes, the presence of a central quasar should enhance the contrast of the filamentary structures by boosting their Ly α emissivity by up to 2 orders of magnitude (Kollmeier et al. 2010). While the giant Ly α nebulae around some quasars may well be explained by such fluorescently glowing accretion streams, these are by no means typical. More high-resolution simulations will be required in order to predict robustly the luminosities and sizes of Ly α fuzz for the lower-mass haloes typical for radio-quiet QSOs.

5. Conclusions

It seems that on average, radio-quiet QSOs are rather unspectacular sources of spatially extended Ly α emission. The non-detection of such Ly α fuzz in 4 of our objects and the marginal detection in one case are all fully consistent with the results of other recent investigations, although even the combined samples are still small.

The spectacularly bright and extended Ly α nebulae discovered around a few quasars (Weidinger et al. 2005; Martin et al. 2014a; Cantalupo et al. 2014) must be probably considered very rare cases. The rarity of this phenomenon may be explained if giant Ly α nebulae are seen only around QSOs that reside in extraordinarily massive haloes.

The observing techniques used to search for Ly α fuzz around QSOs are quite divers, encompassing narrow-band imaging, long-slit spectroscopy, and now also integral field spectroscopy (IFS). In principle, IFS should surpass the other methods by a large margin; in fact, any IFS datacube allows the user to explore both the narrow-band imaging as well as the spectral domain. The limiting factor for most existing optical IFS studies – including the present investigation – is sensitivity and light-collecting area of the available telescopes. This is however about to change, as a new generation of efficient IFS systems is being deployed at 8–10m class telescopes. Of particular interest for the topic of this study is the MUSE instrument, recently commissioned at the ESO Very Large Telescope (Bacon et al. 2014). Its unprecedented sensitivity will make it an optimal discovery machine for Ly α fuzz around quasars. Moreover, the large field of view of MUSE will ensure that there is no longer a danger of sky subtraction removing physical signal from very extended

nebulae with flat radial profiles. It is to be expected that within a relatively short time, the statistics of observed Ly α fuzz around quasars will improve dramatically, turning the emphasis from discovery to the detailed dissection of physical properties.

Acknowledgements. We thank the support staff at Calar Alto observatory for help with the visitor-mode observations. E.C.H. especially thanks Sebastian Kamann and Bernd Husemann for teaching him how to operate the PMAS instrument. For all visual inspections of IFS datacubes mentioned in this paper we used the software QFitsview³ by Ott (2012). All plots were made with matplotlib (Hunter 2007). The color scheme in Fig. 3 is the cubehelix color scheme by Green (2011). We thank Sebastiano Cantalupo for sharing unpublished details about the nebula around UM 287 with us. Finally, we thank the anonymous referee for constructive input.

References

- Adelberger, K. L., Shapley, A. E., Steidel, C. C., et al. 2005, *ApJ*, 629, 636
 Adelberger, K. L., Steidel, C. C., Kollmeier, J. A., & Reddy, N. A. 2006, *ApJ*, 637, 74
 Ahn, C. P., Alexandroff, R., Allende Prieto, C., et al. 2012, *ApJS*, 203, 21
 Alam, S. M. K. & Miralda-Escudé, J. 2002, *ApJ*, 568, 576
 Bacon, R., Vernet, J., Borisiva, E., et al. 2014, *The Messenger*, 157, 13
 Baek, S. & Ferrara, A. 2013, *MNRAS*, 432, L6
 Basu-Zych, A. & Scharf, C. 2004, *ApJ*, 615, L85
 Bergeron, J., Petitjean, P., Cristiani, S., et al. 1999, *A&A*, 343, L40
 Blanc, G. A., Adams, J. J., Gebhardt, K., et al. 2011, *ApJ*, 736, 31
 Bunker, A., Smith, J., Spinrad, H., Stern, D., & Warren, S. 2003, *Ap&SS*, 284, 357
 Cantalupo, S., Arrigoni-Battaia, F., Prochaska, J. X., Hennawi, J. F., & Madau, P. 2014, *Nature*, 506, 63
 Christensen, L., Jahnke, K., Wisotzki, L., & Sánchez, S. F. 2006, *A&A*, 459, 717
 Courbin, F., North, P., Eigenbrod, A., & Chelouche, D. 2008, *A&A*, 488, 91
 Dekel, A., Birnboim, Y., Engel, G., et al. 2009, *Nature*, 457, 451
 Erb, D. K., Bogosavljević, M., & Steidel, C. C. 2011, *ApJ*, 740, L31
 Fanidakis, N., Macciò, A. V., Baugh, C. M., Lacey, C. G., & Frenk, C. S. 2013, *MNRAS*, 436, 315
 Faucher-Giguère, C.-A. & Kereš, D. 2011, *MNRAS*, 412, L118
 Francis, P. J. & Bland-Hawthorn, J. 2004, *MNRAS*, 353, 301
 Francis, P. J. & McDonnell, S. 2006, *MNRAS*, 370, 1372
 Geach, J. E., Smail, I., Chapman, S. C., et al. 2007, *ApJ*, 655, L9
 Goto, T., Utsumi, Y., Walsh, J. R., et al. 2012, *MNRAS*, 421, L77
 Green, D. A. 2011, *Bulletin of the Astronomical Society of India*, 39, 289
 Haiman, Z. & Rees, M. J. 2001, *ApJ*, 556, 87
 Haiman, Z., Spaans, M., & Quataert, E. 2000, *ApJ*, 537, L5
 Hayes, M., Scarlata, C., & Siana, B. 2011, *Nature*, 476, 304
 Heckman, T. M., Lehnert, M. D., Miley, G. K., & van Breugel, W. 1991a, *ApJ*, 381, 373
 Heckman, T. M., Miley, G. K., Lehnert, M. D., & van Breugel, W. 1991b, *ApJ*, 370, 78
 Hennawi, J. F. & Prochaska, J. X. 2013, *ApJ*, 766, 58
 Hennawi, J. F., Prochaska, J. X., Burles, S., et al. 2006, *ApJ*, 651, 61
 Horne, K. 1986, *PASP*, 98, 609
 Humphrey, A., Villar-Martín, M., Fosbury, R., et al. 2007, *MNRAS*, 375, 705
 Humphrey, A., Villar-Martín, M., Fosbury, R., Vernet, J., & di Serego Alighieri, S. 2006, *MNRAS*, 369, 1103
 Hunter, J. D. 2007, *Computing In Science & Engineering*, 9, 90
 Husemann, B., Kamann, S., Sandin, C., et al. 2012, *A&A*, 545, A137
 Husemann, B., Wisotzki, L., Sánchez, S. F., & Jahnke, K. 2013, *A&A*, 549, A43
 Kamann, S., Wisotzki, L., & Roth, M. M. 2013, *A&A*, 549, A71
 Kollmeier, J. A., Zheng, Z., Davé, R., et al. 2010, *ApJ*, 708, 1048
 Martin, D. C., Chang, D., Matuszewski, M., et al. 2014a, *ApJ*, 786, 106
 Martin, D. C., Chang, D., Matuszewski, M., et al. 2014b, *ApJ*, 786, 107
 Matsuda, Y., Yamada, T., Hayashino, T., et al. 2004, *AJ*, 128, 569
 Matsuda, Y., Yamada, T., Hayashino, T., et al. 2011, *MNRAS*, 410, L13
 Nilsson, K. K., Fynbo, J. P. U., Møller, P., Sommer-Larsen, J., & Ledoux, C. 2006, *A&A*, 452, L23
 North, P. L., Courbin, F., Eigenbrod, A., & Chelouche, D. 2012, *A&A*, 542, A91
 Oke, J. B. 1990, *AJ*, 99, 1621
 Ott, T. 2012, QFitsView: FITS file viewer, astrophysics Source Code Library
 Ouchi, M., Ono, Y., Egami, E., et al. 2009, *ApJ*, 696, 1164
 Pâris, I., Petitjean, P., Aubourg, É., et al. 2012, *A&A*, 548, A66
 Prescott, M. K. M., Dey, A., & Jannuzi, B. T. 2012, *ApJ*, 748, 125
 Prescott, M. K. M., Dey, A., & Jannuzi, B. T. 2013, *ApJ*, 762, 38

³ <http://www.mpe.mpg.de/~ott/QFitsView/>

- Rauch, M., Becker, G. D., Haehnelt, M. G., Carswell, R. F., & Gauthier, J.-R. 2013, MNRAS, 431, L68
- Rees, M. J. 1988, MNRAS, 231, 91P
- Roche, N., Humphrey, A., & Binette, L. 2014, MNRAS, 443, 3795
- Rosdahl, J. & Blaizot, J. 2012, MNRAS, 423, 344
- Roth, M. M., Fechner, T., Wolter, D., et al. 2010, in Society of Photo-Optical Instrumentation Engineers (SPIE) Conference Series, Vol. 7742, High Energy, Optical, and Infrared Detectors for Astronomy IV, 774209
- Roth, M. M., Kelz, A., Fechner, T., et al. 2005, PASP, 117, 620
- Saito, T., Shimasaku, K., Okamura, S., et al. 2006, ApJ, 648, 54
- Sánchez, S. F., Aceituno, J., Thiele, U., Pérez-Ramírez, D., & Alves, J. 2007, PASP, 119, 1186
- Sánchez, S. F. & Humphrey, A. 2009, A&A, 495, 471
- Sánchez, S. F., Kennicutt, R. C., Gil de Paz, A., et al. 2012, A&A, 538, A8
- Sandin, C., Becker, T., Roth, M. M., et al. 2010, A&A, 515, A35
- Sandin, C., Weibacher, P., Tabataba-Vakili, F., Kamann, S., & Streicher, O. 2012, in Proceedings of SPIE, Vol. 8451, Software and Cyberinfrastructure for Astronomy II, ed. C. G. Radziwill N. M., Society of Photo-Optical Instrumentation Engineers (SPIE), 84510F
- Schaerer, D. 2003, A&A, 397, 527
- Steidel, C. C., Adelberger, K. L., Shapley, A. E., et al. 2000, ApJ, 532, 170
- Steidel, C. C., Erb, D. K., Shapley, A. E., et al. 2010, ApJ, 717, 289
- Taniguchi, Y. & Shioya, Y. 2000, ApJ, 532, L13
- Telfer, R. C., Zheng, W., Kriss, G. A., & Davidsen, A. F. 2002, ApJ, 565, 773
- Vanden Berk, D. E., Richards, G. T., Bauer, A., et al. 2001, AJ, 122, 549
- Véron-Cetty, M.-P. & Véron, P. 2010, A&A, 518, A10
- Wall, J. V. 1979, QJRAS, 20, 138
- Weidinger, M., Møller, P., & Fynbo, J. P. U. 2004, Nature, 430, 999
- Weidinger, M., Møller, P., Fynbo, J. P. U., & Thomsen, B. 2005, A&A, 436, 825
- Willott, C. J., Chet, S., Bergeron, J., & Hutchings, J. B. 2011, AJ, 142, 186
- Wisotzki, L., Becker, T., Christensen, L., et al. 2003, A&A, 408, 455
- Zirm, A. W., Dey, A., Dickinson, M., & Norman, C. J. 2009, ApJ, 694, L31